http://www.imavs.org/

Design of aeroacoustically stealth MAV rotors

P. Li Volsi* and D. Gomez-Ariza
PARROT Drones SAS, Paris, 75010, France
R. Gojon, T. Jardin and J.-M. Moschetta
ISAE-SUPAERO, Université de Toulouse, Toulouse, 31400, France

ABSTRACT

The more restrictive airspace regulations force drone manufacturers to take into account the noise emitted during the design phase, along with the aerodynamic performance to increase the flight time. Here, a Non-Linear Vortex Lattice Method (NVLM), coupled with the Farassat Formulation-1A of the Ffowcs-Williams and Hawkings acoustic analogy is used to evaluate the aerodynamic and aeroacoustic performance of MAV rotors. Pymoo, a Python-based optimization framework, is employed to modify the geometry, evaluate its performance and extract the set of Pareto optimal solutions. The two objectives are the aerodynamic Figure-of-Merit and the Sound Pressure Level of the 1st Blade Passing Frequency peak for a microphone located in the rotor wake at a far-field distance of 1.62m and 30° from the rotor plane. The approach proposed in this paper takes into account up to ten different parameters, ranging from the twist and chord distributions, to the rake and skew angles.

1 INTRODUCTION

MAV drones are revolutionizing the world with their versatility and controllability. They are employed in the civilian sector by film producers, photographers and, in the near future, by enterprises for delivering goods in urban areas. They share the airspace with helicopters and airplanes but the operability costs and the dimensions of the latter make MAVs a real asset in difficult environments and urban areas (Figure 1 shows two drones used in civil and military sectors). For this reason, MAV usage is steadily increasing every year and they need to comply with new and more restrictive international regulations that include noise emissions and safety. Since in the future they will fly above people, the noise emitted should respect different criteria. Because of the high rotation speed of MAV propellers, their noise is unpleasant for the human hear and this is mainly caused by the highly coupled aerodynamic and aeroacoustic interactions between the rotors[1, 2], and with the drone body[3].

Figure 1: The Parrot ANAFI AI (on the left), the civil version of the Parrot ANAFI USA (on the right). Courtesy of Parrot Drones.

*Email address: pietro.livolsi@parrot.com

Another concern, this time for mission capabilities, comes from their low endurance. The viscous drag induced by the low Reynolds number, at which MAV rotors operate, reduces the aerodynamic efficiency of the rotors, hence reduces the endurance for a given energy storage.
The objective of this paper is to tackle both problems by providing an optimization framework that complies with industrial time and cost constraints. A Non-Linear Vortex Lattice Method, firstly introduced in sections 2.1 and 2.2, then validated in sections 2.3, is used in an optimization loop that exploits the multi-objectives properties of the python framework Pymoo (see section 3.1) to design acoustically and aerodynamically optimized rotors. The optimization results are presented and analyzed in section 4.

2 NUMERICAL METHOD

2.1 Non-Linear Vortex Lattice Method

The Non-Linear Vortex Lattice Method used in this work has been previously presented by Jo et al.[4, 5]. It is based on the incompressible ($\nabla \cdot \mathbf{V} = 0$), inviscid ($\nu = 0$) and irrotational ($\nabla \wedge \mathbf{V} = \mathbf{0}$) flow assumptions. The velocity vector is consequently expressed by the gradient of a potential flow ($\mathbf{V} = \nabla(\phi)$) that satisfies Laplace's equation: $\Delta(\phi) = 0$. These hypothesis allow to simulate complex flows by means of simpler potential flows. The blade is considered thin and its mean camber line is divided into $N_i \times N_j$ lattices whose vortex strengths are noted $\Gamma_{i,j}$.
The rotor wake is also modeled using vortex rings following a prescribed wake geometry. The sectional linear lift is obtained by applying the Kutta-Joukovsky theorem ($L_j = \rho_\infty V_\infty \Gamma_j$). A look-up table procedure is used to take into account the low Reynolds number induced non-linearity and is obtained by means of XFOIL[6] polar calculations. The approach is here used in a steady framework to reduce computational costs and comply with industrial constraints. However, it can be extended to unsteady simulations and free wake models, using free vortex particles to model the wake

http://www.imavs.org/

as shown in Jo et al.[4, 5] (Figure 2 shows the two different simulations).

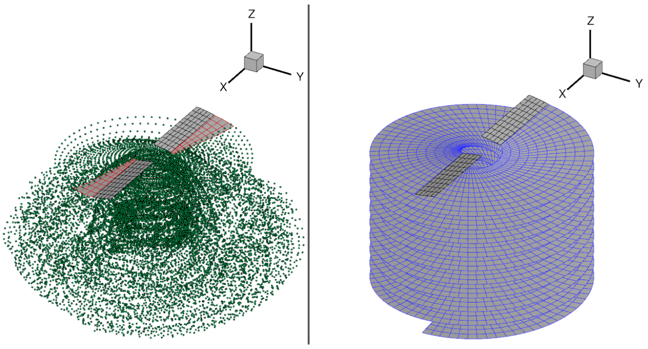

Figure 2: On the left, an unsteady simulation snapshot with Blade lattices, Wake Lattices (the red panels) and Vortex Particles (the green dots). On the right, a steady simulation snapshot with Blade lattices with the Prescribed Wake Lattices (the blue panels).

2.2 *Tonal noise - Farassat Formulation-1A*

The Formulation-1A presented by Farassat [7] has been implemented to the aforementioned Non-Linear Vortex Lattice Method code to capture the tonal noise spectrum emitted by the rotor. The tonal noise, for low-Reynolds and low-Mach number rotors, is generated by two sources:

$$p'(\mathbf{x},t) = p'_T(\mathbf{x},t) + p'_L(\mathbf{x},t) \tag{1}$$

- The thickness noise generated by the displacement of the fluid due to the blade passage, which depends purely on the blade geometry (through the $\mathbf{n}$ normal vector of equation 2) and the rotation speed (through the terms $\mathbf{v}$ and $\mathbf{M}$, that are respectively the absolute speed and the Mach speed of the elementary surface considered);

$$\begin{aligned} 4\pi p'_T(\mathbf{x},t) &= \int_{f=0} \left[\frac{\rho_0(\dot{v}_n + v_{\dot{n}})}{r\left|1-M_r\right|^2} \right]_{ret} dS \\ &+ \int_{f=0} \left[\frac{\rho_0 v_n (r\dot{M}_r + cM_r - cM^2)}{r^2\left|1-M_r\right|^3} \right]_{ret} dS \end{aligned} \tag{2}$$

- The loading noise that is dependent on the unsteady and steady pressure distributions on the blade ($\mathbf{l}$ and $\dot{\mathbf{l}}$ in equation 3) and the rotation speed:

$$\begin{aligned} 4\pi p'_L(\mathbf{x},t) &= \frac{1}{c}\int_{f=0} \left[\frac{\dot{l}_r}{r\left(1-M_r\right)^2} \right]_{ret} dS \\ &+ \int_{f=0} \left[\frac{l_r - l_M}{r^2\left(1-M_r\right)^2} \right]_{ret} dS \\ &+ \frac{1}{c}\int_{f=0} \left[\frac{l_r(r\dot{M}_r + c(M_r - M^2))}{r^2\left(1-M_r\right)^3} \right]_{ret} dS \end{aligned} \tag{3}$$

$$\tau = t - \frac{r}{c} = t - \frac{|\mathbf{x}-\mathbf{y}|}{c} \tag{4}$$

With:

$$l_r = l_i\hat{r}_i \quad \dot{l}_r = \dot{l}_i\hat{r}_i \quad l_M = l_i\hat{M}_i$$

The observer position plays an important role through the $\mathbf{r}$ observer vector and the projection of the other vectors onto this one. Therefore, the inputs needed for the tonal noise calculations are: the observer position, the rotation speed, the pressure distribution on the mean camber line (calculated through the NVLM code and exclusively needed for the loading noise), and the 3D geometry (for the thickness noise).

2.3 *Validation*

To validate the code, unsteady simulations were compared with experiments from Gojon et al.[8] obtained on a two-bladed, NACA12-profiled, 10° constant pitch, constant chord rotor operating at 6000 RPM. Differences of +7.4% and +4.4% on thrust and torque coefficients have been obtained, respectively, which is within the uncertainty typically obtained between experiments with different test benches and different specimen of a given rotor geometry (Deters et al.[9], Gojon et al.[8]). Steady simulations provide comparable results with differences of 11% and 0.9% on thrust and torque coefficients respectively.
In addition, the acoustic simulations were compared to the experimental results of Gojon et al.[8]. As shown in Fig.3, differences lower than 3dB for microphones located in the rotor wake and between 3dB and 6dB for microphones located upstream of the rotor plane were observed. Since MAVs are usually flown above people, acoustic simulation for a microphone at 30° below the rotor is used for the optimizations of section 3. It was here verified that steady simulations provide similar sound pressure levels than unsteady simulations. Hence, because steady simulations are faster than unsteady ones by an order of magnitude, they are used in the optimization procedure to calculate the aerodynamic and acoustic performance of MAV rotors.

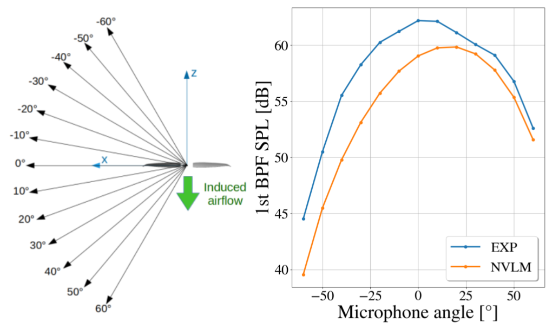

Figure 3: On the left, the microphone locations are displayed; On the right, the comparison between the experimental data and the simulations is shown.

http://www.imavs.org/

3 Optimization

The objective of this paper is to optimize the geometry of an MAV rotor in hovering conditions. The two optimization objectives are: The aerodynamic Figure-Of-Merit [10] $FM = \left(T^{3/2}\right) / \left(\omega Q\sqrt{2\rho\pi R^2}\right)$ and the Sound Pressure Level at the 1st BPF peak for a microphone located at a far-field distance of 1.62m and 30° below the rotor plane, in the direction of the flow. The ideal rotor has a higher Figure-of-Merit for an extended flight endurance and a lower SPL value to be acoustically stealthier.

Previous rotor aeroacoustic, multi-objectives optimizations [11, 12, 13, 14, 15, 16] have shown that, since these two objectives are in conflict, a single solution for this optimization that simultaneously improves both objectives does not exist. Instead, a series of optimal solutions that form a Pareto-front can be calculated. In this section, the optimization framework is presented (subsection 3.1), as long as the optimization algorithm in subsection 3.2, its parameters in subsection 3.3 and the design variables and constraints in subsection 3.4.

3.1 *Pymoo package*

The Python-native optimization framework Pymoo[17] is used in this work. This framework allows to make both single- and multi-objectives optimizations, based on different algorithms, like GA, CMAES, NSGA-II, etc. The reader is referred to reference [17] for further details.

3.2 *Optimization algorithm*

Genetic Algorithms (GA) are inspired by Charles Darwin's theory of natural evolution and based on the survival of the fittest, but also on the appearance of crossover combinations and mutations that can lead to fitter successive generations. Since they work with a population of solutions, different set of solutions can be maintained throughout the optimization and lead more easily to global minima, while gradient-based optimizations can get stuck to local ones. They can also identify the set of Pareto optimal solutions. The main difference between GAs lies in the survival and selection methods.
The NSGA-II (Non-dominated Sorting Genetic Algorithm) [18] was chosen for this study. This algorithm is one of the first genetic algorithm and was opportunely modified from the first version of the code to improve the convergence speed and use the elitism as a way to increase the performance and prevent the loss of good solutions.

3.3 *Optimization setup*

As highlighted in the previous subsection, genetic algorithms like the NSGA-II used in this study require the number of candidates that will be part of the initial population. In this case, a population of 100 candidates has been chosen. The candidates are randomly chosen in order to increase the diversity and the possibility of finding good candidates. The selection is made through the tournament selection method that selects a number of individuals, compares their fitness and selects the parents that will then be modified through the crossover operations and mutations to give birth to the new generation.
The crossover operation used is the "Simulated Binary Crossover" (more details on [19]). This operation, also called recombination, combines the genetic data of different parents to create a newborn.
The mutation operation, instead, randomly modifies the parameters by taking into account a given probability. The mutation probability is here set to zero.

3.4 *Design variables, geometrical reconstruction and constraints*

The rotor geometry on which the optimizations are based is described in table 1:

Rotor parameters	
# of blades	2
Airfoil Section	NACA0012
Diameter [m]	0.25
Root cut-out	15% of the Radius

Table 1: Non-optimized rotor parameters.

The design variables taken into account in the optimization are listed in table 2 along with the minimum and maximum bounds.

Design variables			**Min Value**	**Max Value**
Twist	CP_{twist}	Angle	5°	30°
		Position	20%	80%
	TIP_{twist}	Angle	0°	10°
Chord	CP_{chord}	Length	0.025m	0.075m
		Position	20%	80%
	TIP_{chord}	Length	0.005m	0.05m
Skew	CP_{skew}	Position	20%	80%
	TIP_{skew}	Angle	-10°	10°
Rake	CP_{rake}	Position	20%	80%
	TIP_{rake}	Angle	-10°	10°

Table 2: Design variables used in this work and their minimum and maximum bounds.

A continuous function allows the optimization algorithm to choose the values of each parameter within the minimum and maximum bounds (the number of possible combinations is set by machine precision). Once the ten variables are calculated by the optimization algorithm, the NVLM code builds the new geometry. The chord and twist distributions are defined as follow:

- The root chord and pitch are respectively fixed at 0.025m and 10°;

http://www.imavs.org/

- The $\text{CP}_{chord,pos}$ defines the spanwise position at which the $\text{CP}_{chord,len}$ is applied. The derivative at this point is fixed to zero (same strategy for the twist distribution with $\text{CP}_{twist,pos}$ and $\text{CP}_{twist,ang}$ variables);
- The chord length at the tip of the blade is defined by $\text{TIP}_{chord,len}$ (the pitch at the tip by $\text{TIP}_{twist,ang}$).

Once the interpolation function is defined by the previous points, the geometry is interpolated and 10 spanwise values of the twist angles and the chord lengths are calculated to generate the geometry.
A similar approach for the skew and rake (commonly known as winglet) distributions has been used:

- Both skew and rake angles and their derivatives are equal to zero at the root of the blade;
- The $\text{TIP}_{skew,ang}$ and $\text{TIP}_{rake,ang}$ variables define the angles at the tip;
- The $\text{CP}_{skew,pos}$ is the last point (going from the root to the tip of the blade) to have both skew/rake angles and their derivatives equal to zero.

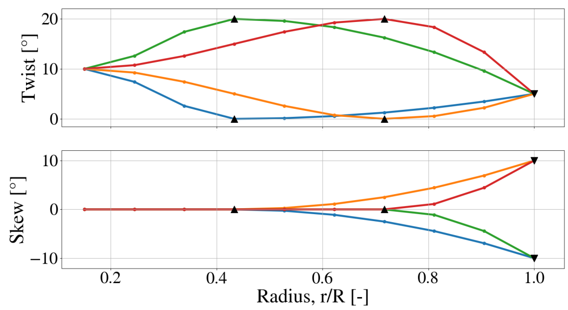

Figure 4: Twist (on top) and skew (on the bottom) distribution definition from the Control point (the black upward pointing triangles) and the tip value (the black downward pointing triangles).

Figure 4 shows, on top, an example of twist distribution interpolation. The upward pointing triangles represent the four control points with two different positions and two different values of the pitch angle, while the downward pointing triangles represent the tip value (for the sake of visibility it was kept constant in the plot). On the bottom an example of skew/rake distribution is presented: in this case both control points (represented by the upward pointing triangles) and angles at the tip (the downward pointing triangles) are changed and 4 different distributions are created.
The NACA0012 airfoil has been kept constant to limit the size of the parameter space.

To optimize both endurance and noise of a ∼800 grams MAV drone, the MAV single-rotor optimization is conducted at 2N iso-thrust. To obtain this thrust value the following procedure has been put in place:

- The algorithm chooses the values of the design parameters and the i^{th} geometry is generated;
- An aerodynamic calculation at 4000RPM is run and the mean thrust calculated;
- By making the assumption that the thrust follows an ideal quadratic function (Thrust $= a \cdot \Omega^2$), the "a" coefficient is calculated and the rotation speed Ω_{2N} deduced[1].
- A new aerodynamic calculation is run and, with it, an acoustic one in order to get the two objective values FM and 1st BPF SPL.
- The two objective values are evaluated by the NSGA-II algorithm.

In the following section, the results of four different optimizations are presented: one optimization does not take into account the rake/skew angles, one takes into account the rake distribution (but not the skew), while another one the skew (but not the rake), and one takes both into account. This helps assess the role of rake and skew on optimal solutions.

4 RESULTS

In this section the results from the aerodynamic and aeroacoustic optimizations of MAV rotors using the genetic algorithm NSGA-II and the non-linear vortex lattice method coupled with the Farassat Formulation-1A solution of the Ffowcs-Williams and Hawkings analogy are presented. As explained in the previous section, two calculations per iteration are needed, which means that for a total of 40 generations (with 100 candidates each), 8000 simulations need to be computed. For this reason, having a low computational cost per simulation is crucial and, therefore, the steady-simulation feature has been preferred over the unsteady counterpart. The NVLM main parameters are summed-up in table 3.

Blade discretization	
# of Chordwise Lattices (N_i)	5
# of Spanwise Lattices (N_j)	10
Simulation parameters	
Revolutions [-]	5
Step angle [°]	5

Table 3: Simulation parameters used for the validation of the NVLM code.

Figure 5 shows the Pareto-fronts obtained with four different optimization setups, including or not rake and skew distributions in the design variables.

[1] within 6% of the target thrust.

http://www.imavs.org/

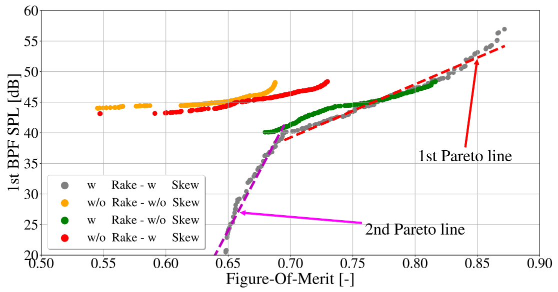

Figure 5: Scatter plot with four different Pareto-fronts and the two Pareto lines.

The orange-colored Pareto-front represents an optimization with only 6 design variables, since it does not include skew and rake variables into the optimization loop. Red and green Pareto-fronts are 8-variables optimizations: they include the skew and rake distributions in the rotor design respectively. This allows to slightly improve the performance of the Pareto set of optimal rotors. It is shown that including the skew variables helps to move the Pareto-front towards better aerodynamic efficiencies but does not yield significant changes in acoustic performance. When the rake variables are introduced in the loop, instead, the optimization seems more appropriate to find aerodynamically ideal rotors and acoustically stealthier ones with 5dB difference with respect to the orange curve. The last optimization, depicted with the grey dots, includes both rake and skew distributions into the design parameters and has the widest Pareto-front, with both aerodynamic and acoustic performance overtaking the ones given by the green-colored rake-included Pareto-front. It also shows two linear trends: the red one (referred to as ”1st Pareto line”) and the magenta one (”2nd Pareto line”). For this reason, only this last optimization run will be presented and analyzed in more details.

The dots of figure 6 scatter plot represent all the candidates of the 10-variables optimization. The green ones, that represent the last generation candidates, are all very close to the Pareto-front and show that the optimization algorithm has converged to the Pareto set of optimal solutions.

As described in subsection 2.2, the total tonal noise depends on two sources (the loading noise and the thickness noise). For this reason it is important to analyze the interaction between them to understand the previous graph. Figure 7 shows four differently coloured Pareto-fronts.

The main results are:

- The rotation speed (figure 7 - top-right scatter plot) changes along the Pareto-front. By following the 1st Pareto line from right to left, the rotation speed increases until the junction between the two Pareto lines. Here, the rotation speed drops suddenly, to increase

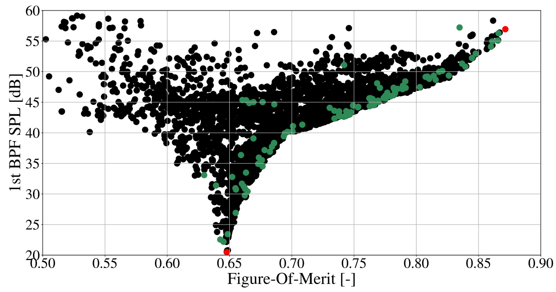

Figure 6: Scatter plot representing all candidates simulated: the last generation candidates in green and the best aerodynamic efficient and the acoustically stealthier candidates in red (whose geometries are shown in figure 12).

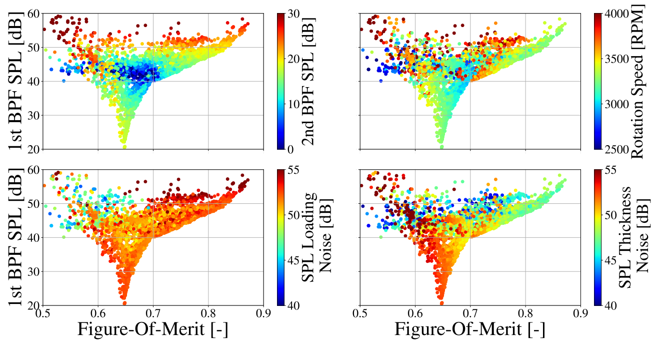

Figure 7: Four scatter plots showing the candidates coloured by different variables.

again along the 2nd Pareto line. While the influence of a reduced rotation speed on the reduction of tonal noise is explicit from equations 3 and 2, these results indicate that it may be counterbalanced by other terms such as rotor solidity (shown in figure 10 and defined as follow: $\sigma = \left(N_{blades} \cdot \overline{chord}\right) / (\pi R)$);

- The thickness noise (figure 7 - bottom-right scatter plot) follows the same trend of the rotation speed. A steady increase from right to left of the first Pareto line is followed by a sudden decrease in the thickness noise level and, again, an increase along the second Pareto line;

- At a far-field microphone location, the loading noise (figure 7 - bottom-left scatter plot) depends mainly on the magnitude of thrust force. However, even for geometries having the same thrust, differences in the order of 3dB are depicted in the graph and depend on the loading distribution, but also on the rotation speed of the rotor (see equation 3);

- The geometries colored by the 2nd BPF SPL (figure 7 - top-left scatter plot) show that optimizing the 1st BPF does not affect, in the same way, the 2nd BPF.

http://www.imavs.org/

Overall, it can be understood from these results that while loading noise dominates the acoustic footprint on the first Pareto line, it is competed by thickness noise on the second Pareto line. An increase in the rotation speed can be compensated for by an increase in rotor solidity to achieve a given target thrust. Furthermore, an increase in rotor solidity increases thickness noise through its explicit contribution in equation 2. Because the thickness noise is weak compared to the loading noise on the first Pareto line, an increase in rotor solidity that significantly impacts the SPL and a reduction in SPL can be directly correlated with a decrease in RPM. Conversely, because the thickness noise is of the same order of magnitude than loading noise on the second Pareto line, an increase in rotor solidity contributes to an increase in SPL (see figure 10). Hence SPL is not solely correlated with RPM, which explains why rotor geometries with lower acoustic footprint may not be obtained at minimum rotation speeds. However, a closer look at the 2nd BPF peaks shows how improving the 1st BPF peak does not mean a consequently improvement of the 2nd one as well.

Figures 8 and 9 show the chord lengths, as well as the pitch, rake and skew angles of the different Control Points (CP) and the Tip (TIP). Here are additional insights on the Pareto optimal solutions:

- The chord at the control point reaches the maximum value allowed to the algorithm. This maximum value is located near the root (see top-left scatter plot of figure 11);
- The chord at the tip (figure 8 - top-right scatter plot) is the key parameter to understand the two Pareto lines: the geometries with higher Figure-Of-Merit have a smaller chord at the tip, which contributes to reduce tip vortex strength. The right Pareto line, instead, presents larger chord lengths at the tip to increase rotor solidity, which may affect thickness/loading noise cancellation mechanisms;
- Rotors with larger aerodynamic efficiency have a higher pitch angle at the control point (see figure 8 - bottom-left scatter plot) because they need to recover the thrust force that is lost by the smaller chord at the tip. The control points are located near the root (see figure 11);
- The pitch at the tip (figure 8 - bottom-right scatter plot) is almost constant everywhere, except on the left side of the first Pareto line. Here, in fact, a higher rotation speed compensates for the lower twist at the tip;
- The rake value is almost constant for all the geometries of the Pareto-front. It points downward, reaches the maximum value and is located very close to the tip. This probably has a double effect: it helps to reduce the torque induced by the tip vortex, and add an outward component to the force vector that changes the phase of both loading and thickness noise, thus reducing the total noise levels;
- The Pareto-front shows two different and opposite skew angles, but the sudden change does not happen on the junction between the two Pareto lines, it happens on the first Pareto line.

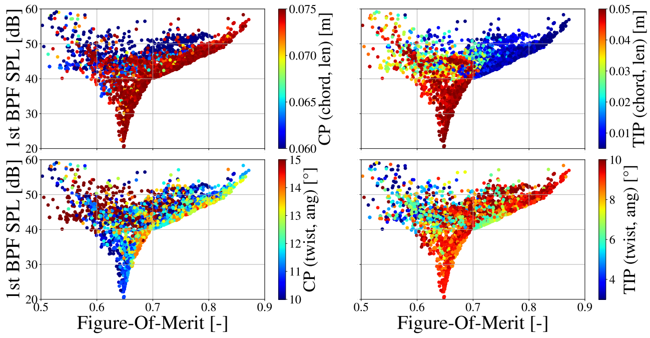

Figure 8: Four scatter plots showing the candidates coloured by design variable values.

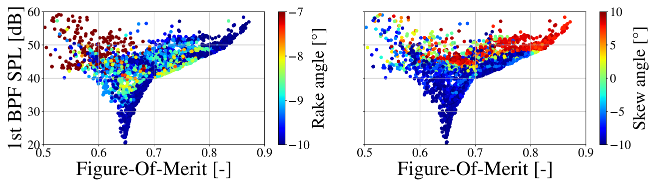

Figure 9: Two scatter plots showing the candidates coloured by rake angle (on the left) and skew angle (on the right) at the tip.

This optimization run shows how three design parameters are important to the improvement of the performance of MAV rotors. The chord length at the tip is the key parameter to understand the two Pareto lines. A smaller chord at the tip can lead to aerodynamically more efficient rotors. Larger ones to acoustically stealthier rotors. The rake and skew distributions play important roles in both aerodynamic and acoustic performance. The former, inducing a downward-pointing blade tip, reaches the maximum values allowed to the algorithm. The skew, instead, deforming the blade in the forward direction for acoustically stealthier rotors and backward for aerodynamically more efficient rotors. The two best geometries are shown in figure 12.

5 CONCLUSION

The approach here presented makes use of a non-linear vortex lattice method, coupled with Farassat's aeroacoustic tonal noise model and the genetic algorithm NSGA-II of

http://www.imavs.org/

Pymoo package to optimize the rotor geometries and find aerodynamically more efficient and aeroacoustically stealthier MAV rotors. The two optimization objectives chosen for this study are the Figure-Of-Merit describing the rotor aerodynamic efficiency and the 1st BPF SPL peak for a microphone located at a far-field distance of 1.62m, at an angle below the rotor plane of 30°. Since drones are generally flown over populated areas and kept at a safety horizontal distance from people, this value of the angle is reasonable. However, the optimization does not take into consideration other angles and, therefore, the influence of the microphone angle will be assessed on future works.

All the optimization runs take into account the twist and chord distributions in the generation of new geometries (the airfoil chosen is the NACA0012), for a total of six design variables. Two optimizations with two additional variables, namely the rake and skew, are independently added. A last optimization run, including all ten design variables, has been performed and has further improved the set of optimal solutions.

The combined effects of both rake and skew on aerodynamic and aeroacoustic performance allowed reaching more efficient and stealthier rotors. The Pareto-front presents two linear trends with different slopes, referred to as Pareto lines. The parameter that splits the two lines is the chord length at the tip. A smaller chord, in fact, is preferable for aerodynamically more efficient rotors while a larger chord gives stealthier rotors.

The negative rake concentrated at the tip pushes the whole Pareto-front to aerodynamically more efficient rotors. Coupling the skew modifications to the rake ones, creates rotors with even higher Figure-Of-Merit and allows to go further on the acoustic counterpart too.

The 1st BPF SPL is only a part of the acoustic spectrum. The acoustic improvements here obtained do not imply improvements over the entire frequency spectrum. In fact, the 2nd BPF peak of the best acoustic configuration is not the lowest value obtained. In addition, if the sensitivity of the human ear is to be considered, the A-ponderation should be applied.

These results are obtained by using the steady simulation capabilities of the NVLM code. However, to validate all the presented results, experimental tests are being prepared at ISAE-SUPAERO. It is also worth noting that this optimization does not take into account the inertia of the blades, the rotation speed at which the motor is more efficient, and the rotor mass. These parameters must be taken into account into future optimizations of commercial MAV rotors.

ACKNOWLEDGEMENTS

This work has been financed by Parrot Drones SAS and the Association Nationale Recherche Technologie (ANRT), realized at ISAE-SUPAERO and performed using HPC resources from GENCI-IDRIS and GENCI-CINES on Jean Zay, Occigen (Grant A0102A07178) and CALMIP on Olympe (Grant 2021-p1425). The authors thank Joseph Morlier and Michael Bauerheim for their insights and advices.

REFERENCES

[1] H. Lee and D. J. Lee. Rotor interactional effects on aerodynamic and noise characteristics of a small multirotor unmanned aerial vehicle. *Physics of Fluids*, 32(4), 2020.

[2] E. J. Alvarez, A. Schenk, T. Critchfield, and A. Ning. Rotor-on-Rotor Aeroacoustic Interactions of Multirotor in Hover. *Journal of the American Helicopter Society*, 2020.

[3] N. S. Zawodny and D. D. Boyd. Investigation of rotor-airframe interaction noise associated with small-scale rotary-wing unmanned aircraft systems. *Annual Forum Proceedings - AHS International*, pages 66–82, 2017.

[4] Y. Jo, H. Lee, and D. J. Lee. Prediction of rotor flow for unmanned aerial system using nonlinear vortex lattice method. *6th Asian-Australian Rotorcraft Forum and Heli Japan 2017, ARF 2017*, 2017.

[5] Y. Jo, T. Jardin, R. Gojon, M. C. Jacob, and J.-M. Moschetta. *Prediction of Noise from Low Reynolds Number Rotors with Different Number of Blades using a Non-Linear Vortex Lattice Method.*

[6] M. Drela. Xfoil: An analysis and design system for low reynolds number airfoils. In Thomas J. Mueller, editor, *Low Reynolds Number Aerodynamics*, pages 1–12, Berlin, Heidelberg, 1989. Springer Berlin Heidelberg.

[7] F. Farassat. Linear acoustic formulas for calculation of rotating blade noise. *AIAA Journal*, 19(9):1122–1130, 1981.

[8] R. Gojon, T. Jardin, and H. Parisot-Dupuis. Experimental investigation of low reynolds number rotor noise. *The Journal of the Acoustical Society of America*, 149(6):3813–3829, 2021.

[9] R. W. Deters, G. K. Ananda, and M. S. Selig. Reynolds number effects on the performance of ailerons and spoilers. *39th Aerospace Sciences Meeting and Exhibit*, (June):1–43, 2001.

[10] G. J. Leishman. *Principles of helicopter aerodynamics / J. Gordon Leishman,...* Cambridge aerospace series. Cambridge University Press, New York, second edition edition, right 2006.

[11] R. Serré, N. Gourdain, T. Jardin, G. Delattre, and J.-M. Moschetta. Analysis of the flow produced by a low-Reynolds rotor optimized for low noise applications. Part II: Acoustics. *43rd European Rotorcraft Forum, ERF 2017*, 2:799–805, 2017.

http://www.imavs.org/

[12] R. Serré, N. Gourdain, T. Jardin, M. C. Jacob, and J.-M. Moschetta. Towards silent micro-air vehicles: optimization of a low Reynolds number rotor in hover. *International Journal of Aeroacoustics*, 18(8):690–710, 2019.

[13] C. Nana, M. Yann, and R. Serré. Fast Multidisciplinary Optimization of a MAV propeller for noise reduction: from simulation to experimentation. *53rd 3AF International Conference on Applied Aerodynamics*, (June), 2018.

[14] C. F. Wisniewski, A. R. Byerley, W. H. Heiser, K. W. Van Treuren, and W. R. Liller. Designing small propellers for optimum efficiency and low noise footprint. *33rd AIAA Applied Aerodynamics Conference*, (June):1–17, 2015.

[15] F. Boyer and A. Drapier. Multidisciplinary optimization of a MAV propeller for noise reduction. pages 301–306, 2017.

[16] G. Wilke. Findings in aero-acoustic simulations for optimizations. In *76th Annual Forum*, Virtual, October 2020.

[17] J. Blank and K. Deb. Pymoo: Multi-objective optimization in python. *IEEE Access*, 8:89497–89509, 2020.

[18] K. Deb, A. Pratap, S. Agarwal, and T. Meyarivan. A fast and elitist multiobjective genetic algorithm: NSGA-II. *IEEE Transactions on Evolutionary Computation*, 6(2):182–197, 2002.

[19] K. Deb, K. Sindhya, and T. Okabe. Self-adaptive simulated binary crossover for real-parameter optimization. In *Proceedings of the 9th Annual Conference on Genetic and Evolutionary Computation*, GECCO '07, page 11871194, New York, NY, USA, 2007. Association for Computing Machinery.

APPENDIX A: RESULTS AND GEOMETRIES

In this appendix three images are presented:

- A scatter plot showing the candidates colored by rotor solidity (figure 10);
- Four scatter plots in figure 11 coloured by the following variables: relative spanwise position of the chord control point (CP$_{chord,pos}$ at top-left), relative spanwise position of the twist control point (CP$_{twist,pos}$ at top-right), relative spanwise position of the rake control point (CP$_{rake,pos}$ at bottom-left) and relative spanwise position of the skew control point (CP$_{skew,pos}$ at bottom-right);
- Three different views (From top to bottom: Z, Y and 3D view) of figure 12 showing two rotors corresponding to the red dots of figure 6.

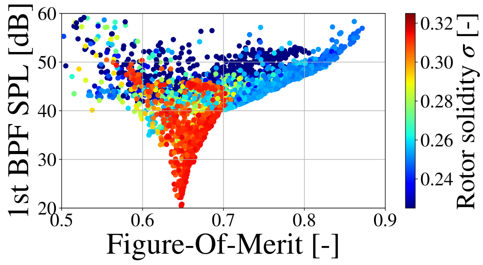

Figure 10: Scatter plot showing the candidates colored by rotor solidity.

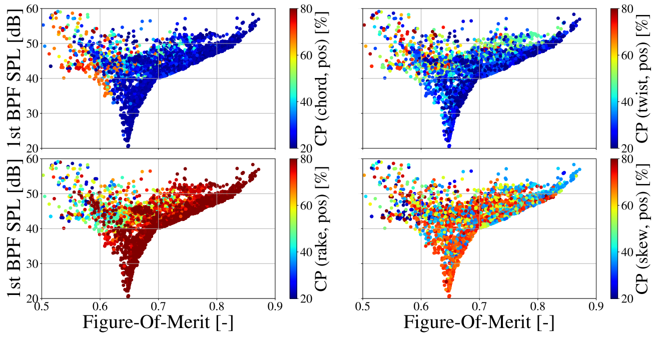

Figure 11: Scatter plot showing the candidates coloured by the control point variables.

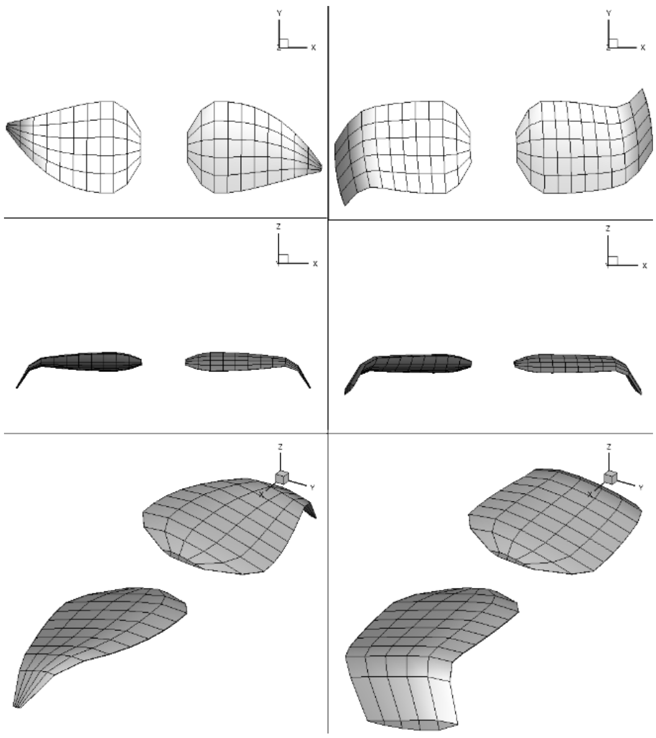

Figure 12: On the left: the rotor with highest Figure-Of-Merit, on the right: with the lowest acoustic footprint.